# Process feedbacks that control transport capacity at formative flows in laterally-constrained gravel-bed rivers: a laboratory study

David Lawson Adams[1] and Brett C Eaton[1]

[1]University of British Columbia

November 24, 2022

## Abstract

In gravel-bed rivers, deterministic approaches to predicting bedload transport use the mean bed shear stress (termed one-dimensional or '1D' equations) or integrate across the frequency distribution of shear stress (2D equations). At low flows, incorporating a range of shear stress values increases prediction accuracy, but at relatively high flows the 1D and 2D approaches are similarly accurate. We contribute to an understanding of the stage-dependent relationship between morphology and bedload transport, and specifically why the mean shear stress characterises transport capacity at formative discharges. We performed physical modelling using a generic Froude-scaled model of a steep laterally-constrained gravel-bed river and captured digital elevation models to perform 2D hydraulic modelling. Both 1D and 2D Meyer-Peter Müller equations were highly accurate across two distinct channel morphologies. In alternate bar channels, transport capacity was controlled by negative feedbacks between flow depth and local bed slope that resulted in a relatively homogeneous distribution of bed shear stress. In plane-bed channels, which lacked the degrees-of-freedom available for large-scale morphologic adjustment, transport capacity was controlled by a spatially variable migrating surface texture. The contrasting spatial patterns of morphology, hydraulics, and surface texture between the two channel morphologies highlight the potential for the same correlation between mean shear stress and transport capacity to emerge through different mechanisms. We suggest that nonlinear feedbacks explain why simple bedload transport equations can be highly effective above a certain flow stage across a range of channel morphologies, and further work should examine whether lateral adjustment confounds this result.

# Process feedbacks that control transport capacity at formative flows in laterally-constrained gravel-bed rivers: a laboratory study

David L. Adams[1,2] and Brett C. Eaton[1]

[1]Department of Geography, University of British Columbia, Canada
[2]School of Geography, Earth and Atmospheric Sciences University of Melbourne, Australia

Corresponding author: David L. Adams
Email: dladams@alumni.ubc.ca
ORCID: 0000-0001-8578-8076

## Key words

- Both 1D and 2D Meyer-Peter Müller equations were highly accurate across two distinct experimental channel morphologies at formative discharges
- The effectiveness of 1D equations at high flows was explained by nonlinear feedbacks between morphology, hydraulics, and sediment transport
- Specifically, in alternate bar channels transport capacity was controlled by negative feedbacks between flow depth and local bed slope

## Abstract

*In gravel-bed rivers, deterministic approaches to predicting bedload transport use the mean bed shear stress (termed one-dimensional or '1D' equations) or integrate across the frequency distribution of shear stress (2D equations). At low flows, incorporating a range of shear stress values increases prediction accuracy, but at relatively high flows the 1D and 2D approaches are similarly accurate. We contribute to an understanding of the stage-dependent relationship between morphology and bedload transport, and specifically why the mean shear stress characterises transport capacity at formative discharges. We performed physical modelling using a generic Froude-scaled model of a steep laterally-constrained gravel-bed river and captured digital elevation models to perform 2D hydraulic modelling. Both 1D and 2D Meyer-Peter Müller equations were highly accurate across two distinct channel morphologies. In alternate bar channels, transport capacity was controlled by negative feedbacks between flow depth and local bed slope that resulted in a relatively homogeneous distribution of bed shear stress. In plane-bed channels, which lacked the degrees-of-freedom available for large-scale morphologic adjustment, transport capacity was controlled by a spatially variable migrating surface texture. The contrasting spatial patterns of morphology, hydraulics, and surface texture between the two channel morphologies highlight the potential for the same correlation between mean shear stress and transport capacity to emerge through different mechanisms. We suggest that nonlinear feedbacks explain why simple bedload transport equations can be highly effective above a certain flow stage across a range of channel morphologies, and further work should examine whether lateral adjustment confounds this result.*



**Key words:** bedload transport, transport capacity, morphodynamics, channel morphology, wavelet transform, gravel-bed rivers

# 1 Introduction

In alluvial systems, there are strong feedbacks between the morphology of a river and the transport of bedload material (Bridge and Jarvis, 1982; Dietrich and Smith, 1983; Church, 2010). Bedload transport and deposition are key processes by which morphology emerges (Church and Ferguson, 2015), but by concentrating flow in preferential paths, the morphology may determine both the spatial distribution and rate of bedload transport (Ferguson, 2003). For a given flow rate, the rate of bedload transport averaged over time may be termed the system's 'transport capacity.'

Equations that aim to predict bedload transport have been developed using both physical models and field data. Most of these are one-dimensional or '1D' as they index the forces that drive bedload entrainment using the reach-averaged shear stress acting on the bed (Shields, 1936; Gomez and Church, 1989). Researchers have sought to improve upon the 1D approach by accounting for the frequency distribution of shear stress (a 2D approach). By incorporating the range of shear stress values, 2D approaches predict bedload transport more accurately at low flows (Paola and Seal, 1995; Paola, 1996; Nicholas, 2000; Ferguson, 2003; Bertoldi et al., 2009; Monsalve et al., 2020). However, under relatively high flow conditions, 1D and 2D approaches are similarly accurate relatively accurate, yielding similar estimates of transport capacity (e.g., Monsalve et al., 2020).

The contrasting performance of these approaches across different discharge stages has been explained by the role of channel morphology (e.g., bars and pools) that controls the spatial distribution of transport. Under low flow conditions, where the threshold of motion may occur at shear stresses around or above the mean, the 1D approach considerably underestimates transport capacity or incorrectly predicts zero transport because active bedload is concentrated in narrow pathways (Davoren and Mosley, 1986; Carson and Griffiths, 1987).

In this investigation, we aim to identify the feedbacks between bedload transport, channel morphology, and hydraulics that explain why transport capacity is well characterised by the mean shear stress at formative discharges. We performed physical modelling using a generic Froude-scaled model of a steep laterally-constrained gravel-bed river and captured digital elevation models to perform 2D hydraulic modelling. The results highlight process interactions that modulate the spatial and temporal distribution of bedload, which have implications for predicting sediment transport and channel behaviour under flood conditions.

**Table 1:** Summary of unit discharges ($Q/W$) used in each phase (P) of experimental Runs a-c.

| | unit discharge $q$ [L/s/m] | | | |
|---|---|---|---|---|
| | P1 | P2 | P3 | P4 |
| Run a | 5.00 | | | |
| Run b | 3.33 | | | |
| Run c | 2.22 | 3.33 | 5.00 | 7.50 |

# 2 Methodology

Experiments were performed in the Adjustable-Boundary Experimental System (A-BES) at the University of British Columbia (Figure 1), a portion of which have been reported by Adams and Zampiron (2020). The A-BES comprises a 1.5 m wide by 12.2 m long tilting stream table, where the experiments were run as generic Froude-scaled models based on 2003 field measurements from Fishtrap Creek in British Columbia, Canada. The channel had a gradient of 0.02 m/m, average bankfull width of 10 m, formative discharge of approximately 7,500 L/s, and bulk $D_{50}$ of 55 mm. With a length scale ratio of 1:25, the A-BES is scaled to within around 30 percent of the prototype, with an initial width of 0.30 m, formative discharge $Q$ of approximately 1.5 L/s, and $D_{50}$ of 1.6 mm ($D_{84}$ = 3.2 mm, $D_{90}$ = 3.9 mm). The sediment mixture comprised natural clasts with a density of around 2,500 kg/m$^3$.

**Figure 1:** Adjustable-Boundary Experimental System (A-BES) at the University of British Columbia, featuring cameras (top-right) and bank control system at a width of 30 cm.

The experiments utilised interlocking landscaping bricks to constrict the channel to various widths $W$ between approximately 0.08–0.60 m. The narrowest setting was selected based on

**Table 2:** Summary of experiments conducted in the A-BES. Length refers to the median length of digital elevation models (DEMs), which generally varies by $\pm$ 0.1 m, and does not include approximately 20–30 cm of bed at the upstream end. DEM count excludes screeded bed. Experiments 1 and 2 are published in Adams and Zampiron (2020).

| Exp | W [m] | L [m] | Q [L/s] | Duration [hrs] | DEMs |
|---|---|---|---|---|---|
| Exp2a | 0.08 | 8.7 | 0.40 | 16 | 24 |
| Exp2b | 0.08 | 8.6 | 0.27 | 16 | 24 |
| Exp1a | 0.30 | 10.8 | 1.50 | 16 | 24 |
| Exp1b | 0.30 | 10.7 | 1.00 | 16 | 24 |
| Exp1c | 0.30 | 10.8 | 0.66, 1.00, 1.50, 2.25 | 8, 4, 4, 4 | 20, 16, 16, 16 |
| Exp3a | 0.45 | 10.8 | 2.25 | 16 | 24 |
| Exp3b | 0.45 | 10.8 | 1.50 | 16 | 24 |
| Exp3c | 0.45 | 10.7 | 1.00, 1.50, 2.25, 3.37 | 8, 4, 4, 4 | 20, 16, 16, 16 |
| Exp4a | 0.60 | 10.8 | 2.00 | 16 | 24 |
| Exp4b | 0.60 | 10.8 | 3.00 | 16 | 24 |
| Exp4c | 0.60 | 10.7 | 1.33, 2.00, 3.00, 4.50 | 8, 4, 4, 4 | 20, 16, 16, 16 |

preliminary experiments where the channel was narrowed until bar formation was suppressed entirely. In addition to the various channel widths, four different unit discharges ($q = Q/W$) were used across the experiments (i.e., discharge was scaled by width) that increased by a factor of 1.5 (Table 1). We conceptualise all four unit discharges as formative as they are capable of forming alternate-bar morphologies in the wider channels. Two constant-discharge runs used the middle two discharges, and one multi-discharge run consisted of the four discharges in increasing order. A full list of experiments is provided in Table 2.

At the beginning of each experiment the bulk mixture was mixed by hand to minimise lateral and downstream sorting, and then the in-channel area was screeded to the height of weirs at the upstream and downstream end using a tool that rolled along the brick surface. The flow was run at a relatively low rate (at which there was little-to-no movement of sediment) until the bed was fully saturated, and was then rapidly increased to the target flow. There was no initial feed of sediment.

Three different types of data were collected throughout each experiment; surface photos, stream gauge measurements, and sediment output. A rolling camera rig positioned atop the A-BES consisted of five Canon EOS Rebel T6i DSLRs with EF-S 18–55 mm lenses positioned at varying oblique angles in the cross-stream direction to maximise coverage of the bed, and five LED lights. Photos were taken in RAW format at 0.2 m downstream intervals, providing a stereographic overlap of over two-thirds. Ten water stage gauges comprised of a measuring tape (with 2 mm intervals) on flat boards were located along the inner edge of the bricks every 1 m (but every 0.8 m for the 0.08 m experiments due to the slightly shorter length). To minimise edge effects, gauges were not placed within 0.60 m of either the inlet or the outlet. Also, the gauges were read at an almost horizontal angle, which in conjunction with the dyed blue water, minimised systematic bias towards higher readings due to surface tension effects. Based on the measurement precision of the stream gauge readings, errors of 6—11 percent could be expected for mean hydraulic depths (relative errors are variable due to different depths).

The data collection procedure was designed to maximise measurement accuracy as much as was reasonably possible. Given that stream gauge data would later be paired with topographic data, the timing of gauge readings needed to closely coincide with surface photography (i.e., so there was as little morphologic change as possible between the time gauges were read and the time the bed was captured). Every time photos were taken the bed was drained, as the surface water would distort the photos. These constraints necessitated a procedure in which manual stream gauge readings (to the nearest 1 mm) were taken 30–40 seconds before the bed being rapidly drained (around the minimum time it would take to obtain the readings), after which the bed was photographed and gradually re-saturated before resuming the experiment (approximately 10 minutes).

Each experimental phase was divided into a series of segments between which the data collection procedure would occur. The procedure occurred in 5, 10, 15, 30, 60, and 120 minute segments with four repeats of each (i.e., 4 x 5 min, 4 x 10 min), which was designed to reflect the relatively rapid rate of morphologic change at the beginning of each phase. For example, in wider channels, alternate bars developed within an hour, and there was relatively little morphologic change in the following hours (Adams and Zampiron, 2020).

Throughout the experiments, sediment falling over the downstream weir was collected in a mesh bucket, drained of excess water, weighed damp to the nearest 0.2 kg, placed on the conveyor belt at the upstream end, and gradually recirculated at the same rate it was output (gas opposed to a ‘slug’ injection). Based on a range of samples collected across the experiments, we determined the weight proportion of water to be approximately 5.8 percent and applied this correction factor to obtain approximate dry weights. Zero sediment was fed into the system during the first 5-minute phase. The experiments are best described as pseudo-recirculating as sediment was fed at the end of each segment, and every 15 minutes regardless of whether the bed was drained.

## 2.1 Data processing

Using the images, point clouds were produced using structure-from-motion photogrammetry in Agisoft MetaShape Professional 1.6.2 at the highest resolution, yielding an average point spacing of around 0.25 mm. Twelve spatially-referenced control points (and additional unreferenced ones) were distributed throughout the A-BES, which placed photogrammetric reconstructions within a local coordinates system and aided in the photo-alignment process. Using inverse distance weighting, the point clouds were converted to digital elevation models (DEMs) at 1 mm horizontal resolution. Despite the use of control points, the DEMs contained a slight arch effect (an artefact of the processing) whereby the middle of the model (in a downstream direction) was bowed upwards. This effect was first quantified by applying a quadratic function along the length of the bricks, which represent an approximately linear reference elevation (brick elevations vary by $\pm$ 4 mm). The arch was then removed by determining correction values along the length of the DEM using the residuals, which were then applied across the width of the model.

For each DEM, ten wetted cross-sections were reconstructed using the water surface elevation data, which were then used to estimate reach-averaged hydraulics. For more detailed spatial analysis, the flow conditions (water depth, shear stress) were reconstructed using a 2D numerical flow model (Nays2DH) to the final DEM of each discharge phase. To minimise rounding errors associated with the relatively shallow depths in the stream table and the grid size, the DEM size and discharge were adjusted to the prototype scale (i.e., using a length scale of 25) for the flow modelling. The estimated water depths, shear stresses and velocities from Nays2DH were then back-transformed to the model scale (Table 3). We removed cells with relatively shallow flow to eliminate non-active channel areas, defined as depths less than $2D_{84}$. The mean-normalised frequency distributions of shear stress were fit with a Gamma distribution, where the goodness-of-fit was statistically significant (P $<$ 0.05) based on both Kolmogorov-Smirnov and Anderson-Darling tests. Shape $\alpha$ and rate $\beta$ parameters for the Gamma distributions were highly correlated and only the former is presented here (Table 4).

To account for spatial variability of surface texture, without specific measurements of flow resistance, flow modelling was conducted twice for a given surface. First, we used a constant Manning's n value of 0.045, and second, a spatially variable value that was back-calculated using the flow resistance law presented by Ferguson (2007). A flow duration of 100 seconds was sufficient to establish convergence. The results of the flow model were quantitatively validated by comparing measured reach-averaged hydraulic depths ($h = A/w$, where $A$ is flow cross-sectional area and $w$ is wetted width) to modelled ones (Figure 2). Most estimates fall within 10–15 percent of the line of equality, although the flow model estimates a narrower range of mean flow depths across the experiments. The flow model is likely a more accurate estimate of flow depths compared to the stream gauge measurements as they are easily biased towards either large or small values due to the relatively small sample size.

**Table 3:** Summary of mean hydraulics from Nays2DH models for the final DEM of each discharge phase. Flow depth is $d$, and Reynolds number $Re = Ud/v$, where $v$ is the kinematic viscosity.

| Exp | $w$ [m] | $d$ [m] | $U$ [m/s] | Fr [-] | $\bar{\tau}$ [Pa] | Re [-] |
|---|---|---|---|---|---|---|
| Exp2a | 0.07 | 0.016 | 0.36 | 0.92 | 2.47 | 4431 |
| Exp2b | 0.07 | 0.013 | 0.30 | 0.85 | 2.18 | 3026 |
| Exp1a | 0.26 | 0.015 | 0.36 | 0.93 | 2.68 | 4155 |
| Exp1b | 0.22 | 0.013 | 0.31 | 0.85 | 2.39 | 3166 |
| Exp1c(1) | 0.18 | 0.012 | 0.28 | 0.81 | 2.07 | 2556 |
| Exp1c(2) | 0.22 | 0.013 | 0.30 | 0.81 | 2.26 | 2997 |
| Exp1c(3) | 0.26 | 0.016 | 0.35 | 0.88 | 2.85 | 4167 |
| Exp1c(4) | 0.28 | 0.018 | 0.44 | 1.03 | 3.35 | 6127 |
| Exp3a | 0.48 | 0.015 | 0.34 | 0.87 | 2.69 | 3873 |
| Exp3b | 0.34 | 0.014 | 0.33 | 0.87 | 2.45 | 3613 |
| Exp3c(1) | 0.28 | 0.013 | 0.30 | 0.83 | 2.18 | 3027 |
| Exp3c(2) | 0.37 | 0.013 | 0.31 | 0.83 | 2.35 | 3190 |
| Exp3c(3) | 0.45 | 0.015 | 0.35 | 0.89 | 2.69 | 4090 |
| Exp3c(4) | 0.52 | 0.017 | 0.41 | 0.97 | 3.22 | 5400 |
| Exp4a | 0.56 | 0.015 | 0.35 | 0.89 | 2.73 | 3975 |
| Exp4b | 0.46 | 0.013 | 0.31 | 0.82 | 2.28 | 3188 |
| Exp4c(1) | 0.36 | 0.013 | 0.31 | 0.84 | 2.11 | 3129 |
| Exp4c(2) | 0.46 | 0.014 | 0.32 | 0.85 | 2.33 | 3391 |
| Exp4c(3) | 0.54 | 0.015 | 0.37 | 0.93 | 2.79 | 4377 |
| Exp4c(4) | 0.67 | 0.017 | 0.41 | 0.97 | 3.09 | 5413 |

## 2.2 1D and 2D sediment transport equations

We compared the observed mean transport rate over the last three hours of each experiment (twelve measurements at intervals of 15 min) to predictions from two sediment transport equations (1D and 2D). This approach assumes that the spatial distribution of shear stress remained relatively similar over the averaging period, which is supported by the lack of morphologic change and relatively stable mean hydraulics as estimated by gauge measurements. We used the Meyer-Peter and Müller (1948) equation (MPM)

$$q_s = k(\bar{\tau} - \tau_c)^{1.6} \tag{1}$$

where $q_s$ is width-averaged sediment transport, and Wong and Parker (2006) estimate that $k$ = 4.94. The parameter $\bar{\tau}$ is the mean shear stress, and the critical shear stress value is defined as $\tau_c = \theta_c g(\rho_s - \rho)D$, where $\theta_c$ is the dimensionless critical shear stress, $g$ is gravity, $\rho$ is the density of water, $\rho_s$ is the density of sediment, and $D$ is the grain size (median size $D_{50}$

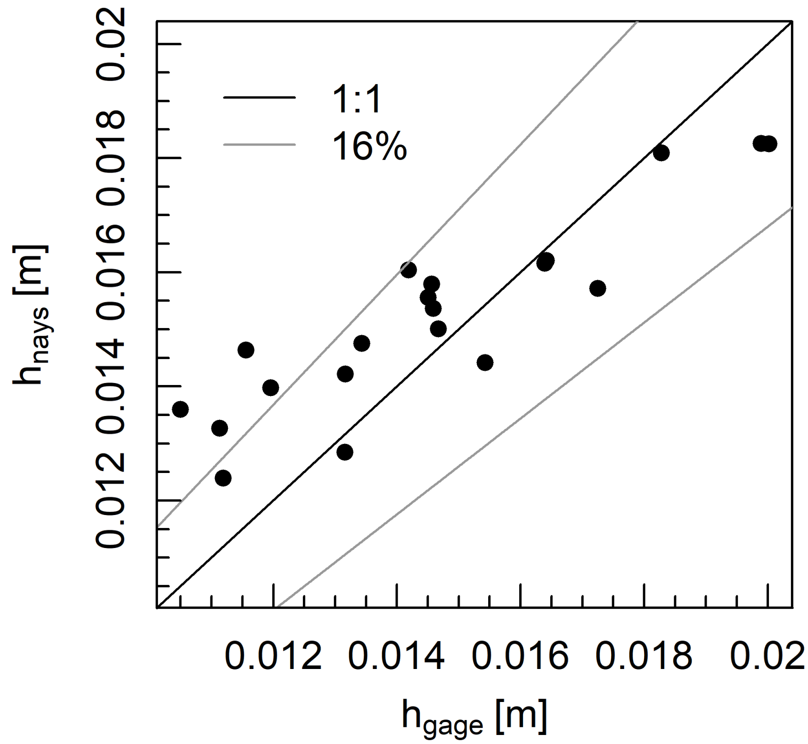


**Figure 2:** Measured versus modelled mean hydraulic depth $h$ at the end of each experimental phase, featuring 16 percent bounds.

is used here). This 1D equation may be divided into flows greater than or less than the critical shear stress and expressed as

$$\begin{aligned} q_{s(x)} &= k(\tau_{(x)} - \tau_c)^{1.6} \qquad (\text{for } \tau_{(x)} > \tau_c) \\ &= 0 \qquad (\text{for } \tau_{(x)} \leq \tau_c) \end{aligned} \tag{2}$$

and a 2D approach is derived by integrating across a known frequency distribution of shear stress

$$q_s = k \int (\tau_{(x)} - \tau_c)^{1.6} dx \tag{3}$$

These 1D and 2D equations provide width-averaged estimates of sediment transport using reach-averaged shear stress (Equation 1) and the entire frequency distribution of shear stress ($q_{b,\bar{\tau}}$ and $q_{b,f(\tau)}$, respectively). In the 1D approach, we optimised the values of $\theta_c$ and the coefficient $k$ based on a non-linear least-squares approach. This provided values of 0.053 and 3.4, respectively, which were then used for the 2D equation. A summary of experimental results is presented in Table 4.

**Table 4:** Summary of experimental results with sediment transport emphasis. Units: $\tau$ [Pa], $q_b$ [kg/m/s]. For each experiment, all parameters represent mean values derived from the final DEM or associated Nays2DH model, except for $q_b$ which is averaged over three hours.

| Exp | $w/d$ | $\bar{\tau}$ | $q_b$ | $q_{b,\bar{\tau}}$ | $q_{b,f(\tau)}$ | $\alpha$ |
|---|---|---|---|---|---|---|
| Exp2a | 4.60 | 2.47 | 1.06 | 1.35 | 2.20 | 5.39 |
| Exp2b | 5.40 | 2.18 | 0.16 | 0.63 | 1.21 | 8.59 |
| Exp1a | 17.5 | 2.68 | 1.75 | 1.98 | 3.36 | 3.87 |
| Exp1b | 16.3 | 2.39 | 0.97 | 1.13 | 2.52 | 3.25 |
| Exp1c(1) | 15.3 | 2.07 | 0.34 | 0.43 | 1.50 | 3.13 |
| Exp1c(2) | 16.8 | 2.26 | 0.86 | 0.81 | 2.20 | 2.46 |
| Exp1c(3) | 16.6 | 2.85 | 1.81 | 2.56 | 4.09 | 3.72 |
| Exp1c(4) | 15.4 | 3.35 | 3.68 | 4.54 | 5.86 | 5.99 |
| Exp3a | 32.2 | 2.69 | 2.48 | 1.99 | 3.61 | 2.85 |
| Exp3b | 23.9 | 2.45 | 1.10 | 1.29 | 2.61 | 3.16 |
| Exp3c(1) | 21.6 | 2.18 | 0.53 | 0.64 | 1.69 | 3.31 |
| Exp3c(2) | 27.7 | 2.35 | 1.21 | 1.04 | 2.40 | 3.10 |
| Exp3c(3) | 29.7 | 2.69 | 2.01 | 2.01 | 3.71 | 2.60 |
| Exp3c(4) | 30.2 | 3.22 | 4.34 | 3.96 | 5.86 | 3.36 |
| Exp4a | 37.8 | 2.73 | 2.42 | 2.15 | 3.87 | 2.97 |
| Exp4b | 34.0 | 2.28 | 1.14 | 0.86 | 2.28 | 2.18 |
| Exp4c(1) | 27.4 | 2.11 | 0.49 | 0.50 | 1.60 | 2.49 |
| Exp4c(2) | 33.2 | 2.33 | 1.22 | 0.97 | 2.38 | 3.01 |
| Exp4c(3) | 35.0 | 2.79 | 2.52 | 2.35 | 3.83 | 2.90 |
| Exp4c(4) | 38.5 | 3.09 | 4.41 | 3.44 | 4.62 | 5.96 |

## 2.3 Analysing longitudinal scaling patterns

To explain the spatial patterns of entraining forces we compare the spatial patterns of local bed slope and flow depth that give rise to shear stress. To quantify and compare these patterns we use wavelet transform, which decomposes signals into oscillations occurring at different wavelengths (Torrence and Compo, 1998). Specifically, we use the maximal overlap discrete wavelet transform (MODWT) which has been used in a similar application (Adams and Zampiron, 2020). Using the results from the hydraulic model, we located the primary flow path by identifying the highest shear stress at each cross-section, which was then smoothed in a downstream direction by removing spatial outliers and applying a moving average (an example is presented in Figure 4). This longitudinal transect, representing the primary flow path, was then used to extract downstream profiles of local shear stress, bed slope, and flow depth.

# 3 Results

The experiments spanned a range of mean bed shear stresses and width-depth ratios, which are presented in Figure 3. The middle two phases of the multiple-discharge experiments (circled), and the two constant discharge experiments which share the same imposed unit discharge and maximum width, developed similar width-depth ratios and mean shear stress values. For the same unit discharge, the mean shear stress of the 0.08 m experiments was lower compared to the wider experiments due to the sidewall effect whereby there was energy loss to the lateral boundaries.

3).

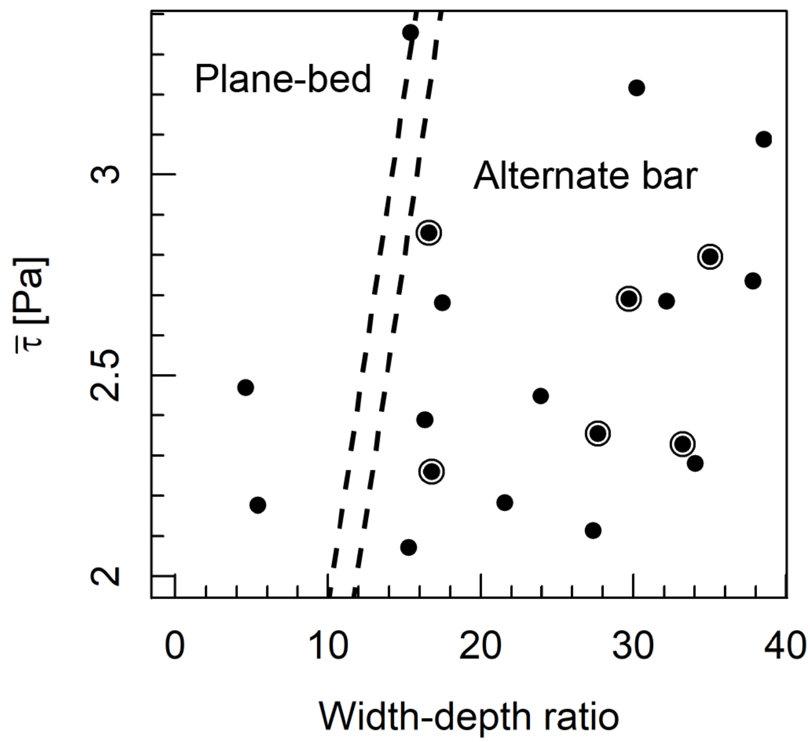


**Figure 3:** Mean bed shear stress and width-depth ratio at the conclusion of each experimental phase, estimated using the flow models. Circled points represent experimental phases 2 and 3 of the multiple discharge experiments which have the same imposed unit discharge and maximum width as the constant discharge experiments (Table 1). Dashed lines indicate approximate transition zone between plane-bed and alternate bars based on our experimental results, as well as width-depth ratio and excess shear stress thresholds summarised by (Rhoads and Welford, 1991).

With increasing width-depth ratio there was a transition from a plane-bed to an alternate bar morphology, and an example is presented in Figure 4 for the latter. In contrast, channel morphology was less sensitive to shear stress (or unit discharge) for a given channel width. As discharge was increased, there was an increase in bar wavelength and at the highest flow, the morphology was more topographically subdued. For simplicity, we classify the experiments into two groups based on morphology: 1) plane-bed channels comprising both 0.08 m wide channels and the highest discharge 0.30 m wide channel, and 2) alternate bar channels (Figure 3).

We observed different spatial patterns of surface texture across the experiments. Plane-bed

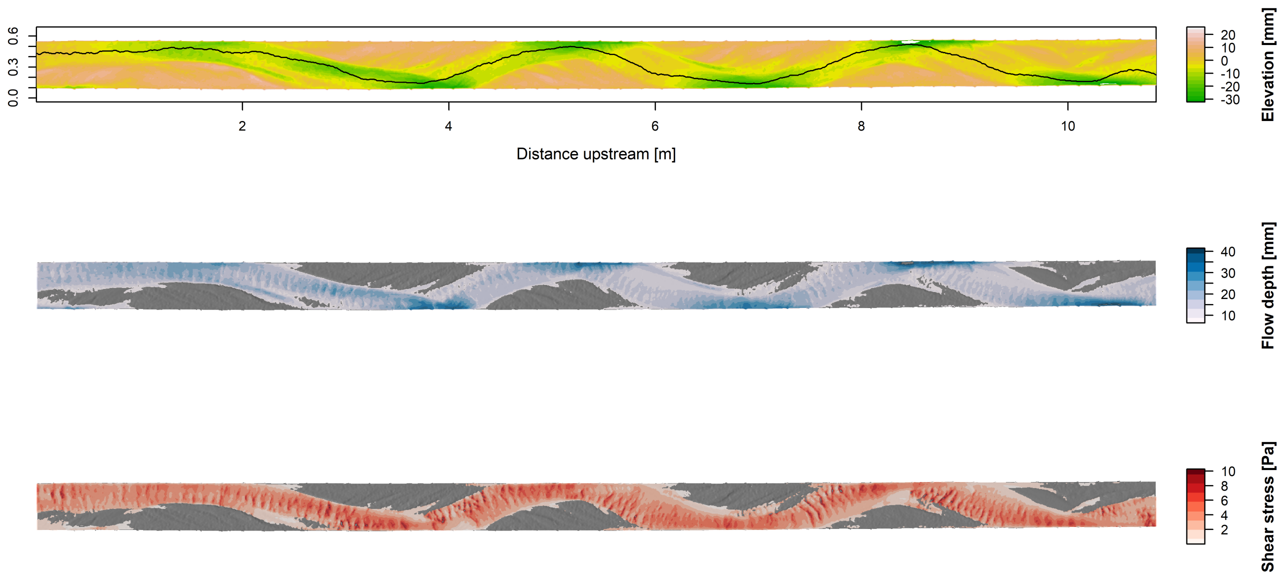


**Figure 4:** Channel area at the conclusion of Experiment 3b ($W$ = 0.45 m, $\bar{\tau}$ = 2.41 Pa) displaying characteristics (top to bottom): a) elevation, b) flow depth, and c) shear stress. Cells where $d < 2D_{84}$ have been removed from the hydraulic model. Thalweg transect is displayed as a black line.

channels were characterised by only longitudinal sorting patterns (alternating coarse and fine patches), whereas in the alternate bar channels fine patches were located around the channel thalweg and coarse patches were concentrated away from the primary flow path.

## 3.1 Longitudinal scaling patterns

In this section, we apply a wavelet transform to describe the longitudinal scaling patterns of flow depth, local bed slope, and shear stress along the primary flow path. The results of this analysis are presented in two ways: 1) the variance of each wavelength, and 2) the cumulative distribution of variance showing the relative contribution of each scale to the total.

At wavelengths shorter than 0.1 m, plane-bed and alternate bar morphologies are indistinguishable based on the variance in flow depth, local bed slope, and shear stress. Differences emerge at longer wavelengths, where in the plane-bed channels there is considerably less variance in flow depth and local bed slope, compared to the more topographically variable alternate bar channels. These contrasting scaling patterns are evident in both the absolute and cumulative representations, which show two groupings of channels. In the longer wavelength scaling patterns of shear stresses the binary grouping gives way to a graded distribution, in which there is less variation in narrow channels compared to wider ones.

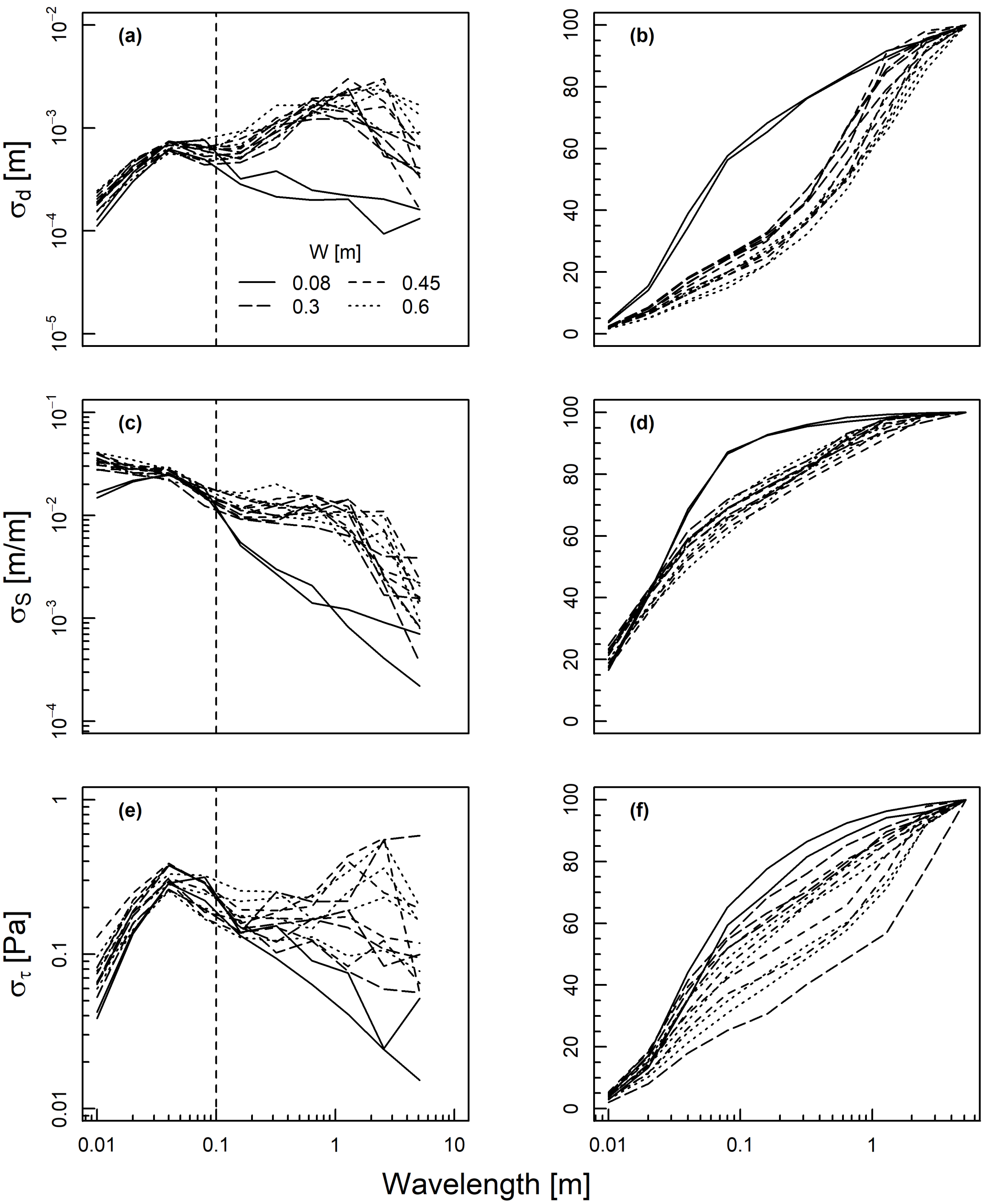


**Figure 5:** Scaling patterns of standard deviation in local flow depth, bed slope, and shear stress for each unique experimental phase, presented as both absolute (a, c, e) and cumulative values (b, d, f), respectively. For brevity, phases 2 and 3 of the multiple discharge experiments are not shown (circled points in Figure 3), so only experiments with unique unit discharge and maximum width combinations are presented. The line style refers to the channel width, and the vertical dashed line refers to the scale below which all channel follow similar scaling patterns.

## 3.2 Spatial concentration of flow

The two morphologic types are well distinguished by their mean-normalised frequency distributions of flow depths (Figure 6a). Plane bed channels have peaked distributions of depths with relatively short tails, whereas alternate bar channels have broader distributions corresponding to areas of relatively shallow and deep flow. This grouping is also evident in the normalised frequency distributions of shear stress, the difference between them is lesser (Figure 6b). The two plane-bed channels, as well as the channel with subdued bars, have Gamma distributions with larger shape and rate parameters (Table 4), which is consistent with their distributions being less positively skewed and more peaked, respectively. There is no systematic variation between the shape of the distribution and the mean shear stress.

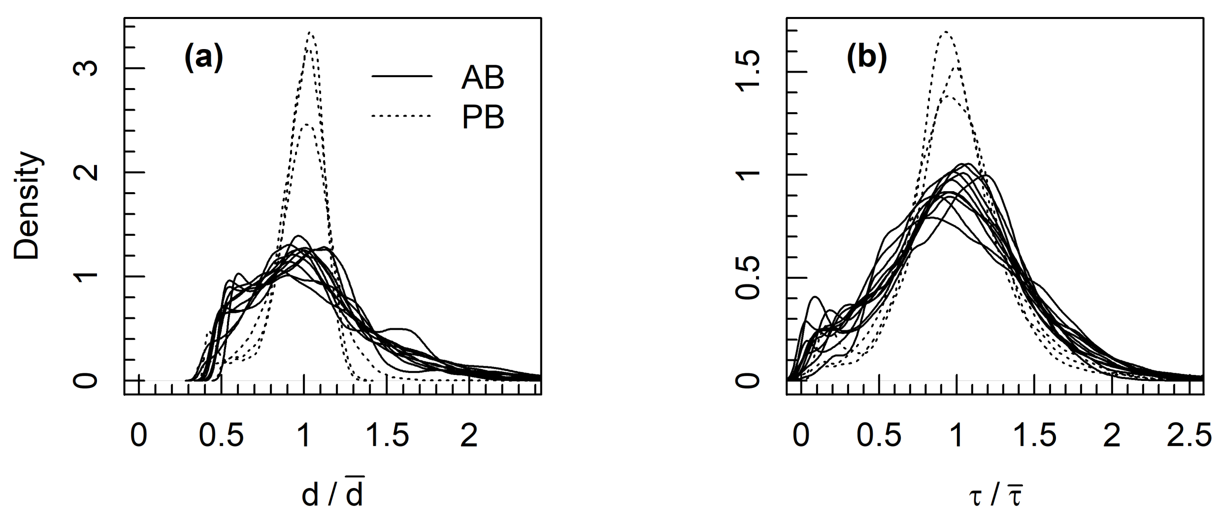


**Figure 6:** Frequency distribution of mean-normalised flow depth and shear stress at the end of each unique experimental phase (see Figure 5 for note on excluded data). AB and PB correspond to alternate bar and plane-bed morphology, respectively. Note the absence of shallow depths which have been removed during data processing to eliminate non-active channel areas.

## 3.3 Sediment transport

All experiments reached a steady-state sediment transport rate whereby individual measurements oscillated around a mean value, although temporal patterns of transport varied between channel morphologies. We present a comparison between two channels with contrasting sources and magnitudes of fluctuations, but similar transport capacities when averaged over time (Figure 7). In the plane-bed example, the presence of coarse and fine patches of sediment produced a spatially variable transport rate, and their downstream migration (i.e., position relative to the outlet) resulted in oscillating volumes of sediment output, ranging from approximately 0.0–3.0 kg/m/min under steady-state conditions. In alternate bar example, bedload transport had less variation through time, ranging from approximately 0.75–1.75 kg/m/min, which was likely associated with morphologic activity at the bar-scale.

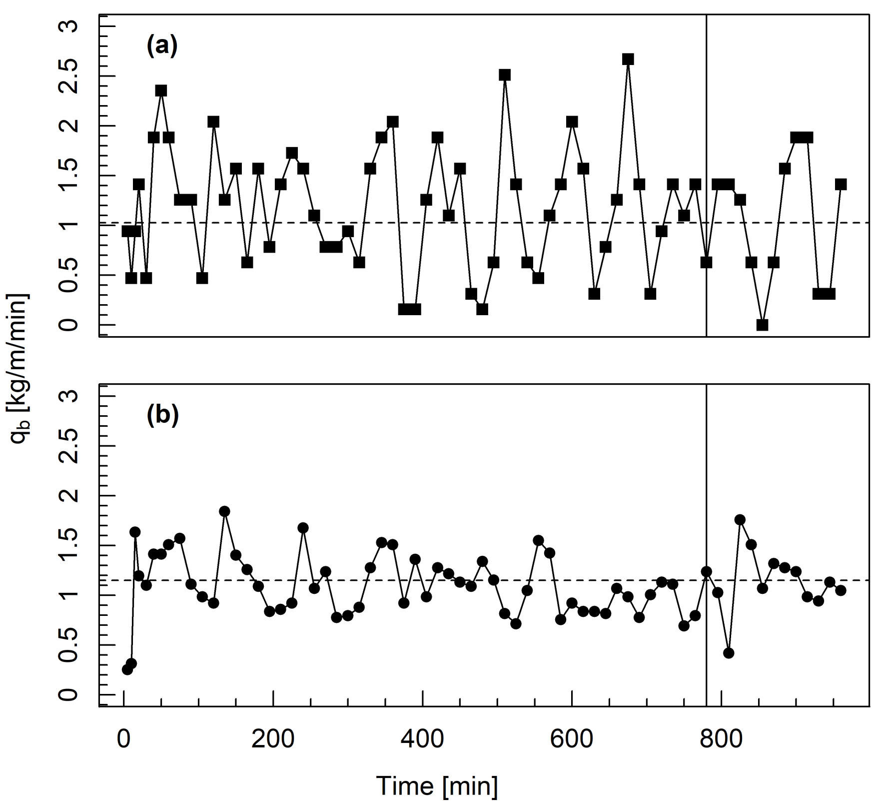


**Figure 7:** Width-averaged bedload transport over time in two experiments with different widths but similar reach-averaged shear stress and transport capacity: a) Experiment 2a (W = 0.08 m, $\bar{\tau}$ = 2.45 Pa), and b) Experiment 4b (W = 0.60 m, $\bar{\tau}$ = 2.22 Pa). The beginning of the time window over which bedload transport is averaged is indicated by the solid vertical line, and mean transport over this period is indicated by a horizontal dashed line.

We compare observed time-averaged sediment transport to predictions made by two versions of the MPM equation, which represent 1D (Equation 1) and 2D (Equation 3) approaches (Figure 8). The 1D approach was calibrated using the coefficient $k$ and the critical value $\tau_c$, and therefore predictions are located along the line of equality. Using the same coefficients the 2D predictions lie approximately parallel to but at an intercept above the line of equality. However, both methods predict sediment transport almost equally well ($R^2$ = 0.89 & 0.90, RMSE = 0.38 & 0.42, respectively), yielding strong correlations between observed and predicted $q_b$.

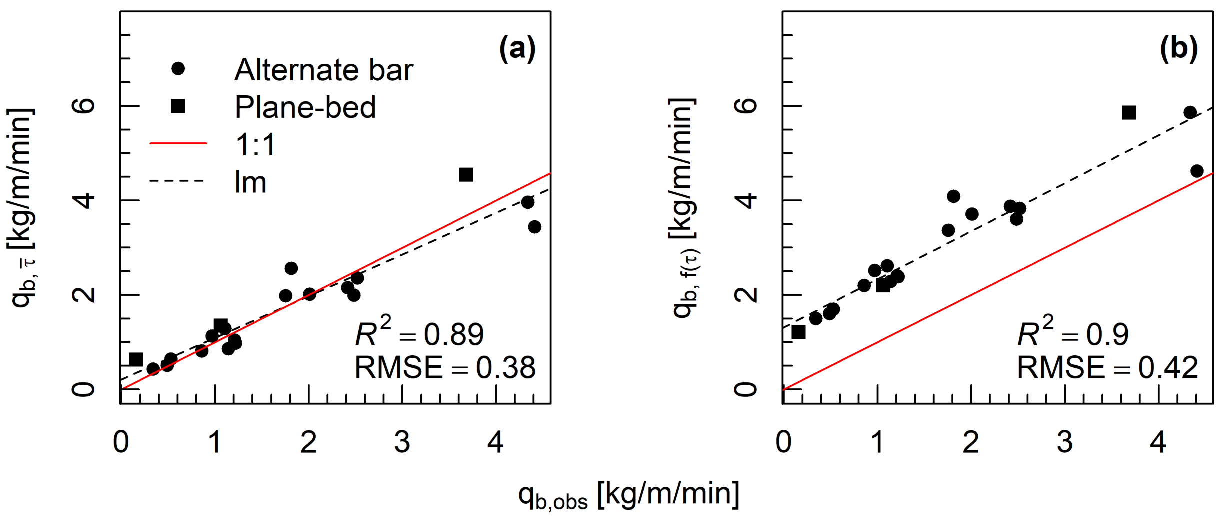


**Figure 8:** Observed vs predicted sediment transport in each experiment, where the time- and width-averaged bedload transport rate $q_b$ is predicted using two MPM equations; a) Equation 1 (1D) and Equation 3 (2D). The dashed black line is least-squares best fit, the red solid line corresponds to a 1 : 1 relation between observed and predicted volumes, and point type refers to morphology.

# 4 Discussion

## 4.1 Width-depth ratio and channel character

The suite of experiments, comprising width-depth ratios from 5–45, and mean bed shear stress values approximately 2–3.3 Pa, produced two primary channel morphologies. With increasing width-depth ratio, there was a transition from plane-bed to alternate bar. With increasing mean shear stress, there was an increase in bar wavelength (and decrease in amplitude) such that channels with the highest unit discharge had a more subdued morphology. The development of alternate bars in wider channels with lower excess shear stresses is supported by several investigations (Fujita, 1989; Garcia Lugo et al., 2015; Carbonari et al., 2020; Rhoads and Welford, 1991). Notably, our experiments conform to the threshold $w/d \approx 10$ (Chang et al., 1971; Ikeda, 1984).

The spatial patterns of morphology and surface texture were coupled. Plane-bed channels exhibited only longitudinal variation in surface texture, with alternating coarse, intermediate, and fine patches, similar to Iseya and Ikeda's (1987) observations of congested, transitional, and smooth states. The spatial distribution of surface texture in alternate bar morphologies was characterised by a repeated pattern of relatively coarse bars and a fine thalweg. This is the reverse of patterns typically observed in sinuous channels, where bars form by the deposition of fine sediment as flow separation arises at bends. This process cannot occur as the fixed straight channel prevents meandering, and under these conditions, bars can only develop via the deposition of large grains. Subsequently, the experiments presented here best replicate processes in relatively straight or confined reaches in nature.

The mean-normalised frequency distributions of shear stress followed Gamma distributions, whose shape varied across the two morphologies. The Gamma distribution shape has been observed in meandering (Segura and Pitlick, 2015; Monsalve et al., 2020) and braided (Nicholas, 2003) channels, although, in contrast to the analysis herein, these results were obtained by modelling a range of flows over the same bathymetry (i.e., the channel boundary could not adjust). In the alternate bar channels, the frequency distribution of shear stress was more positively skewed and less peaked with heavier tails, indicated by lower $\alpha$ and $\beta$ parameters. Previous studies have observed both positive (Segura and Pitlick, 2015) and negative (Monsalve et al., 2020) correlations between flow strength and $\alpha$, whereas there was no correlation in these experiments. These conflicting results may indicate that the relationship between the distribution of $\tau$ and flow strength is more dependent on the specific shape of the channel.

## 4.2 Decoupling of flow depth and shear stress

Alternate bar and plane-bed morphologies were strongly differentiated by their frequency distributions of flow depth (Figure 6). The former was characterised by broad distributions as the flow was associated with pools and riffles, comprising areas of relatively deep and shallow flow, respectively. Although the two morphologies could be distinguished based on the frequency distribution of shear stress, the difference was more subtle as shear stress was relatively spatially homogeneous in the alternate bar morphology, which is evident in the hydraulic maps (Figure 4).

Using the wavelet transform it is possible to describe how the differences between shear stress and flow depth manifest at different spatial scales. Across the suite of experiments, scaling patterns of local bed slope, flow depth, and shear stress were almost identical at wavelengths less than 0.10 m (Figure 5). Differences between experiments emerged on larger scales, where scaling patterns of local bed slope and flow depth were grouped by morphology. However, the scaling patterns of bed shear stress were less distinct between the two morphologies and, rather, there was a gradient of variance at longer wavelengths between them. Thus, both frequency distributions and scaling patterns highlight a decoupling of flow depth and shear stress between the two morphologies at relatively large spatial scales. This result challenges the commonly held assumption that local deviations from $\tau \propto d$ tend to cancel out so that their frequency distributions are similar (Nicholas, 2000; Ferguson, 2003; Bertoldi et al., 2009).

There were similarities in the scaling patterns of local bed slope, flow depth, and shear stress across all experiments (Figure 5a,c). There were almost identical patterns of variance at shorter wavelengths and large differences at longer wavelengths, and the wavelengths that separated these two scaling regions was always located around 0.10 m. The consistency of this scaling boundary across the three parameters is explained by their co-dependency, although its existence may be ascribed to more fundamental processes. The presence of two distinct scaling regions highlights a process decoupling whereby grain-scale processes appear only indirectly related to ones operating at the channel scale. This characteristic of natural self-organised systems has been discussed in the context of the emergence perspective in geomorphology (Werner, 2003; Murray, 2007). The theory describes an indirect relationship between processes operating at different spatio-temporal scales, where the behaviour of the emergent aspects of the system (the morphology) is decoupled from the behaviour of system constituents (the grains). Thus, our experiments provide evidence that supports a hierarchical view of processes and forms in geomorphic systems.

### 4.3 Feedbacks that control transport capacity

Under the relatively high discharges modelled in our experiments, transport capacity was well predicted by both 1D and 2D Meyer-Peter Müller equations based on the strength of the correlation. This result is consistent with previous investigations concerned with the performance of bedload transport equations across various stages (Bertoldi et al., 2009; Monsalve et al., 2020), and suggests that under formative discharges where most geomorphic change occurs 1D approaches may be sufficient to provide accurate estimates of sediment transport, provided that the data is averaged over a long enough period (Recking et al., 2012). Several studies have observed that at low flows morphology (via the spatial concentration of shear stress) acts to increase transport capacity, and the effectiveness of the 1D approach herein supports the notion that the strength of this effect is inversely proportional to the flow stage (Paola and Seal, 1995; Paola, 1996; Nicholas, 2000; Ferguson, 2003).

The specific processes that underlie the stage-dependent relationship between morphology and bedload transport are not yet clear, although our experiments shed light on some important morphodynamics. In the alternate bar channels, transport capacity (via the spatial distribution of shear stress) was likely controlled by a negative feedback between flow depth and local bed slope. The primary flow path encountered alternating positive and negative slopes (associated with pool heads and tails), and their correlation at approximately the scale corresponding to pool spacing is evident in the scaling patterns of flow depth and local bed slope (Figure 5). The interaction between these two parameters acts to reduce shear stress where flow is deepest, and constrains the maximum shear stress across the active channel. This explains both the relatively homogeneous spatial distribution of shear stress compared to flow depth (Figure 4), and the convergence of frequency distributions of shear stress for both alternate bar and plane-bed channels (Figure 6).

The negative feedback between flow depth and local slope indicates that at high flow stages channels may tend to expend excess flow energy and shear stress via the development of morphology. At lower flows, bedload transport is slaved to morphology because the system lacks surplus energy to instrument the morphologic change necessary for such a negative feedback.

Moreover, it is interesting that the plane-bed channels (especially the 0.08 m width) had a similar transport capacity to the alternate bar channels, despite lacking the same degrees-of-freedom available for morphologic adjustment. Instead, in the narrowest channels, bedload transport arose via the longitudinal distribution of surface texture that controlled the threshold for entrainment. The initiation of transport coincided with the concentration of fine sediment into relatively homogeneous downstream migrating patches, which also caused considerably larger fluctuations in output compared to the alternate bar channels (Figure 7). Integrated across space and time, these migrating patches gave rise to a similar transport capacity to the alternate bar for the same mean shear stress. The contrasting spatial patterns of morphology, hydraulics, and surface texture across the experiments highlights the potential for transport capacity to be equifinal under formative discharges.

Both the experiments and bedload transport equations presented herein have limitations that provide opportunities for further research. By constraining channel pattern and preventing lateral adjustment, the fixed-bank experiments also restrict channel processes. More mobile-bank experiments are required to understand how feedbacks between channel processes give rise to the system's transport capacity. By using only the frequency distribution, so-called 2D equations remove the spatial dimension of transport and are only quasi-2D. Processes of sediment entrainment, transport, and disentrainment are affected by local conditions that control the trajectories of grains downstream, and further research must aim to account for this.

# 5 Conclusion

We compared the performance of 1D and 2D bedload transport equations under formative discharge conditions. These flows are particularly relevant for river management as they encompass large volumes of transport and geomorphic change. Physical models with varying channel width-depth ratios and discharges (but identical reach-averaged gradients and bulk grain sizes) produced a range of emergent morphologies and steady-state transport capacities under recirculating conditions. Transport capacity was well predicted by both 1D and 2D Meyer-Peter Müller equations, which is consistent with previous studies indicating that 1D equations may be effective under high discharge conditions when measurements are appropriately temporally averaged.

Our experiments contribute to an understanding of the stage-dependent relationship between morphology and bedload transport, and specifically why the mean shear stress characterises transport capacity so effectively at formative discharges. In channels capable of building bars, the relationship may be explained by a negative feedback between flow depth and local bed slope. This feedback results in a spatial distribution of shear stress that is relatively homogeneous compared to flow depth, and restricts the maximum shear stress available across the active channel. Despite lacking the same degrees-of-freedom available for morphologic adjustment, narrower plane-bed channels maintained the same relationship between transport capacity and mean shear stress via a spatially variable migrating surface texture. The contrasting spatial patterns of morphology, hydraulics, and surface texture between the two channel morphologies highlight the potential for similar system properties to emerge through entirely different mechanisms.

The effectiveness of 1D bedload transport equations in channels where there are feedbacks between channel morphology, sediment transport, and hydraulics highlights the potential for non-linear dynamics to drive linear behaviour. This aspect of fluvial systems explains why simple deterministic equations can be highly effective under certain conditions. Further work is required to examine how additional processes such as lateral adjustment affect morphodynamics.

# Open Research

Raw hydraulic and sediment transport data from Tables 3-4 and Figures 2-3 & 6-8 are available at Zenodo [DOI: 10.5281/zenodo.5750653] with an Open license (Adams, 2021).

# Acknowledgements

We would like to thank Lucy MacKenzie and Will Booker for providing insightful feedback on the manuscript at various stages. This work was supported by graduate scholarships provided by the Canadian and Australian Governments, and a postgraduate writing-up award (Albert Shimmins Fund) from the University of Melbourne.

# References

Adams, D. L. (2021), 'Primary data for submission to Water Resources Research', *Zenodo, DOI: 10.5281/zenodo.5750653* .

Adams, D. L. and Zampiron, A. (2020), 'Short communication: Multiscalar roughness length decomposition in fluvial systems using a transform-roughness correlation (TRC) approach', *Earth Surface Dynamics* **8**, 1039–1051.

Bertoldi, W., Ashmore, P. E. and Tubino, M. (2009), 'A method for estimating the mean bed load flux in braided rivers', *Geomorphology* **103**(3), 330–340.
**URL:** *https://linkinghub.elsevier.com/retrieve/pii/S0169555X08002936*

Bridge, J. S. and Jarvis, J. (1982), 'The dynamics of a river bend: a study in flow and sedimentary processes', *Sedimentology* **29**, 499–542.

Carbonari, C., Recking, A. and Solari, L. (2020), 'Morphology, Bedload, and Sorting Process Variability in Response to Lateral Confinement: Results From Physical Models of Gravel bed Rivers', *Journal of Geophysical Research: Earth Surface* **125**(12).
**URL:** *https://onlinelibrary.wiley.com/doi/10.1029/2020JF005773*

Carson, M. A. and Griffiths, G. A. (1987), 'Bedload transport in gravel channels', *Journal of Hydrology* **26**(1), 1–151.

Chang, H. Y., Simons, D. B. and Woolhiser, D. (1971), 'Flume experiments on alternate bar formation', *Journal of Waterways, Harbors and Coastal Engineering Division* **97**, 155–165.

Church, M. A. (2010), 'The trajectory of geomorphology', *Progress in Physical Geography* **34**(3), 265–286.

Church, M. A. and Ferguson, R. I. (2015), 'Morphodynamics: Rivers beyond steady state', *Water Resources Research* **51**(4), 1883–1897.
**URL:** *https://onlinelibrary.wiley.com/doi/abs/10.1002/2014WR016862*

Davoren, A. and Mosley, M. P. (1986), 'Observations of bedload movement, bar development and sediment supply in the braided Ohau river', *Earth Surface Processes and Landforms* **11**(6), 643–652.
**URL:** *https://onlinelibrary.wiley.com/doi/10.1002/esp.3290110607*

Dietrich, W. E. and Smith, J. D. (1983), Processes controlling the equilibrium bed morphology in river meanders., *in* C. Elliot, ed., 'River Meandering', American Society of Civil Engineers, New York, NY, pp. 759–769.

Ferguson, R. I. (2003), 'The missing dimension: effects of lateral variation on 1-D calculations of fluvial bedload transport', *Geomorphology* **56'**(1-2), 1–14.

Ferguson, R. I. (2007), 'Flow resistance equations for gravel- and boulder-bed streams', *Water Resources Research* **43**(5), 1–12.

Fujita, Y. (1989), Bar and channel formation in braided strams, *in* S. Ikeda and G. Parker, eds, 'River Meandering. American Geophysical Union Water Resources Monographs 12', pp. 417–462.

Garcia Lugo, G. A., Bertoldi, W., Henshaw, A. J. and Gurnell, A. M. (2015), 'The effect of lateral confinement on gravel bed river morphology', *Water Resources Research* **51**(9), 7145–7158.
**URL:** *http://doi.wiley.com/10.1002/2015WR017081*

Gomez, B. and Church, M. A. (1989), 'An Assessment of Bed Load Sediment Transport Formulae Bed Rivers', *Water Resources Research* **25**(6), 1161–1186.

Ikeda, S. (1984), 'Prediction of alternate bar wavelength and height', *Journal of Hydraulic Engineering* **110**, 371–386.

Iseya, F. and Ikeda, H. (1987), 'Pulsations in bedload transport rates induced by a longitudinal sediment sorting: A flume study using sand and gravel mixtures', *Geografiska Annaler. Series A. Physical Geography* **69**(1), 15–27.

Meyer-Peter, E. and Müller, R. (1948), Formulas for bed-load transport, *in* 'Proceedings of the 3rd Meeting of the International Association for Hydraulic Structures Research', Stockholm, Sweden, pp. 1–26.

Monsalve, A., Segura, C., Hucke, N. and Katz, S. (2020), 'A bed load transport equation based on the spatial distribution of shear stress-Oak Creek revisit', *Earth Surface Dynamics* **8**(3), 825–839.

Murray, A. B. (2007), 'Two Paradigms in Landscape Dynamics: Self-Similar Processes and Emergence', *Nonlinear Dynamics in Geosciences* pp. 17–35.

Nicholas, A. P. (2000), 'Modelling bedload yield braided gravel bed rivers', *Geomorphology* **36**(1-2), 89–106.

Nicholas, A. P. (2003), 'Investigation of spatially distributed braided river flows using a two-dimensional hydraulic model', *Earth Surface Processes and Landforms* **28**(6), 655–674.
**URL:** *https://onlinelibrary.wiley.com/doi/10.1002/esp.491*

Paola, C. (1996), Incoherent structure: turbulence as a metaphor for stream braiding, *in* P. J. Ashworth, S. J. Bennett, J. L. Best and S. J. McLelland, eds, 'Coherent flow structures in open channels', Wiley, Chichester, U.K., pp. 705–723.

Paola, C. and Seal, R. (1995), 'Grain size patchniness as a cause of selective deposition and downstream fining', *Water Resources Research* **31**(5), 1395–1407.

Recking, A., Liebault, F., Peteuil, C., Joliment, T., Etgr, U. R. and Martin, S. (2012), 'Testing bedload transport equations with consideration of time scales', *Earth Surface Processes and Landforms* **789**, 774–789.

Rhoads, B. L. and Welford, M. R. (1991), 'Initiation of river meandering', *Progress in Physical Geography* **15**(2), 127–156.

Segura, C. and Pitlick, J. (2015), 'Coupling fluvial-hydraulic models to predict gravel transport in spatially variable flows', *Journal of Geophysical Research: Earth Surface* **120**(5), 834–855.
**URL:** *http://doi.wiley.com/10.1002/2014JF003302*

Shields, A. (1936), 'Application of similarity principles and turbulence research to bed-load movement. Translated to English by W. P. Ott and J. C. van Uchelen).', *Mitteilungen der Preussischen Versuchsanstalt fur Wasserbau und Schifbau, Berlin* **26**(5-24), 47.

Torrence, C. and Compo, G. P. (1998), 'A practical guide to wavelet analysis', *Bulletin of the American Meteorological society* **79**(1), 61–78.

Werner, B. T. (2003), ‘Modeling landforms as self-organized, hierarchical dynamical systems’, *Geophysical Monograph Series* **135**(i), 133–150.

Wong, M. and Parker, G. (2006), ‘Reanalysis and Correction of Bed-Load Relation of Meyer-Peter and Müller Using Their Own Database’, *Journal of Hydraulic Engineering* **132**(11), 1159–1168.